AGU PUBLICATIONS

JGR

Journal of Geophysical Research: Atmospheres

RESEARCH ARTICLE
10.1002/2014JD022751

Key Points:
- Antarctic gravity waves experience significant dissipation from 35 to 105 km
- Slope of GW wave number spectra at 78°S is shallower than lower latitudes
- Wave dissipation rates and wave number spectra vary from stratosphere to MLT

Correspondence to:
X. Lu and X. Chu,
Xian.Lu@colorado.edu;
Xinzhao.Chu@colorado.edu

Citation:
Lu, X., X. Chu, W. Fong, C. Chen, Z. Yu, B. R. Roberts, and A. J. McDonald (2015), Vertical evolution of potential energy density and vertical wave number spectrum of Antarctic gravity waves from 35 to 105 km at McMurdo (77.8°S, 166.7°E), *J. Geophys. Res. Atmos.*, *120*, 2719–2737, doi:10.1002/2014JD022751.

Received 22 OCT 2014
Accepted 9 MAR 2015
Accepted article online 11 MAR 2015
Published online 10 APR 2015

Vertical evolution of potential energy density and vertical wave number spectrum of Antarctic gravity waves from 35 to 105 km at McMurdo (77.8°S, 166.7°E)

Xian Lu[1], Xinzhao Chu[1,2], Weichun Fong[1,2], Cao Chen[1,2], Zhibin Yu[1,2], Brendan R. Roberts[1,3], and Adrian J. McDonald[4]

[1]Cooperative Institute for Research in Environmental Sciences, University of Colorado Boulder, Boulder, Colorado, USA, [2]Department of Aerospace Engineering Sciences, University of Colorado Boulder, Boulder, Colorado, USA, [3]National Ecological Observatory Network, Boulder, Colorado, USA, [4]Department of Physics and Astronomy, University of Canterbury, Christchurch, New Zealand

Abstract We report the first characterization of potential energy densities and vertical wave number spectra of Antarctic gravity waves (GWs) from 35 to 105 km, derived from Fe lidar temperature measurements at McMurdo (77.8°S, 166.7°E) in 2011–2013 winters. For GWs with periods of 2–10 h, the potential energy density per unit volume (E_{pv}) decreases by 2 orders of magnitude from 35 to 105 km, while that per unit mass (E_{pm}) increases from several to hundreds of J/kg. E_{pm} increases with a mean scale height of ~10.4 km in the Rayleigh region (35–65 km) and of ~13.2 km in the Fe region (81–105 km), and of particular interest is the inferred severe dissipation in between (65–81 km). Overall, the vertical evolutions of E_{pv} and E_{pm} indicate considerable wave energy loss from the stratosphere to the lower thermosphere. The vertical wave number spectra exhibit power law forms for vertical wavelengths $\lambda_z <$ ~10 km. The mean spectral slope in the spectral range of 2–10 km is about −2.55 and −2.26 in the Rayleigh and Fe regions with standard deviations of 0.36 and 0.38, respectively. Large variations in the power spectral densities (PSDs) are seen for $\lambda_z >$ 10 km in 35–60 km. PSDs increase by 1 order of magnitude from the stratosphere to the lower thermosphere. Using higher temporal resolution data to include 0.5–2 h waves increase E_{pm} by ~25–45% and increase PSDs of 2–5 km waves by a factor of 2 and of >10 km waves by less than 50%.

1. Introduction

It has been known for decades that gravity waves play an important role in the middle and upper atmosphere since the seminal work by *Hines* [1960], who attributed the large *E* region wind perturbations to internal gravity waves. Since then, gravity waves have been recognized for their dominant contributions to the residual circulation and thermal structure of the mesosphere and lower thermosphere (MLT) region [*Lindzen*, 1981; *Holton*, 1982; *Garcia and Solomon*, 1985; *Fritts and Alexander*, 2003]. Gravity waves are usually generated in the lower atmosphere, and without wave dissipation, their amplitudes increase exponentially with altitude by the scale height of the atmospheric density. As gravity waves dissipate and/or break, wave energies are damped via conversion into turbulent motions and deposition into the mean flow. The vertical evolution of gravity wave potential energy density (GW-E_p) is an important indicator of where and to what extent wave energy is dissipated. This knowledge can help evaluate gravity wave influences on the mean flow and provide guidance for general circulation models to parameterize gravity wave effects.

Various mechanisms have been proposed to account for wave dissipation and saturation, such as convective and shear instability [*Dewan and Good*, 1986; *Smith et al.*, 1987], diffusive damping [*Weinstock*, 1990], diffusive filtering [*Gardner*, 1994], and wave-induced Doppler spreading [*Hines*, 1991, 1997a, 1997b]. However, the question of which mechanism is dominant is still controversial. This controversy leads to the fundamental differences of the various theories attempted to explain the so-called "canonical" wave spectra, i.e., in the spectral region where waves are regarded as being saturated, the power spectral density (PSD) follows a form of m^{-p} (m is the vertical wave number and $-p$ is the slope of the power law and has typical values ranging from −2.5 to −3); in the region dominated by unsaturated waves (usually low m part), PSD follows the source spectrum characteristics [*Van Zandt*, 1982; *Smith et al.*, 1987; *Gardner*, 1994]. The form of m^{-p} is the so-called power law of wave number. The characteristic wave number m^* is the turning point between

these two distinct spectral regions and normally corresponds to the largest wave energy. The wave spectra and associated variations with altitude and environment characterize how wave energy is distributed with wave number and varies with altitude and location. It provides an important framework to develop a useful parameterization of gravity wave drag and diffusion in the lower and middle atmosphere, which is key to general circulation models simulating realistic background temperatures and winds in the middle atmosphere.

Although GW-E_p and wave number spectrum have been studied for decades using Rayleigh, Sodium (Na) and Iron (Fe) lidars [e.g., *Senft and Gardner*, 1991; *Wilson et al*., 1991a, 1991b; *Whiteway and Carswell*, 1994, 1995; *Gardner and Yang*, 1998; *Gardner et al*., 1998; *Gao et al*., 1998; *Yamashita et al*., 2009; *Yang et al*., 2010; *Alexander et al*., 2011a] and radars [e.g., *Tsuda et al*., 1989; *Fritts et al*., 1988; *Sato*, 1994; *McDonald et al*., 1998], most of these studies have focused on either the stratosphere or the mesopause region separately. Far fewer studies have been dedicated to both regions, but these were mainly performed at low and middle latitudes [e.g., *Beatty et al*., 1992; *Senft et al*., 1993; *Rauthe et al*., 2006, 2008; *Lu et al*., 2009]. Thus, the studies of GW-E_p and spectra with a large altitude range at high latitudes are currently missing. However, the gravity wave momentum fluxes from satellite observations and several climate models have shown strong latitudinal variations [*Geller et al*., 2013]. The multistation radiosonde observations have also illustrated that the wave number spectral slopes become shallower with increasing latitude in the stratosphere [*Allen and Vincent*, 1995; *Pfenninger et al*., 1999]. Therefore, studies of GW-E_p and wave number spectra at high latitudes, such as McMurdo, with a large vertical extent are required.

The Fe Boltzmann/Rayleigh temperature lidar at McMurdo (77.8°S, 166.7°E), Antarctica, is one of the best ground-based instruments to observe gravity waves (GWs) over a large altitude range with decent vertical and temporal resolution. A case study using simultaneous lidar and radar measurements at McMurdo/Scott Base has already demonstrated salient signatures of inertial gravity waves (IGWs) from below 35 to 107 km [see *Chen et al*., 2013, Figure 1]. The Fe lidar observations on 28 May 2011 at McMurdo have also clearly shown a gravity wave with a period of 1.5–2 h from 35 to 155 km [*Chu et al*., 2011b, 2012]. During the three winter seasons from 2011 to 2013, the Fe lidar has collected a large amount of data, providing an invaluable opportunity to study the characteristics of GW-E_p and wave number spectrum statistically from the stratosphere all the way to the lower thermosphere.

Such statistical analysis is important in characterizing the forcing of Antarctic gravity waves. As the modeling work [e.g., *McLandress et al*., 2012; *Tan et al*., 2011] and the satellite observations [e.g., *Alexander and Grimsdell*, 2013] suggested, the missing gravity wave drag likely from orographic GWs or IGWs is a strong candidate for the long-lasting "cold pole" problem in climate models for Antarctica. Therefore, a better understanding of the polar wave dissipation and forcing from observations can help solve this problem and lead to a better simulation of climate change, ozone depletion processes, and the recovery of the ozone hole [*McDonald et al*., 2009; *Alexander et al*., 2011b].

2. Lidar Observations

The University of Colorado lidar group has been conducting lidar observations at Arrival Heights (77.83°S, 166.67°E) near McMurdo Station on Ross Island since December 2010 [*Chu et al*., 2011a, 2011b]. The Fe Boltzmann lidar deployed in the campaign is capable of temperature measurements during both day and night, leading to full diurnal data coverage. Detailed principles and instrumentation of this lidar can be found in *Chu et al*. [2002], and its refurbishment and upgrade are discussed in *Wang et al*. [2012]. Temperatures were derived from 30–70 km using the Rayleigh integration technique [*Hauchecorne and Chanin*, 1980] and from 80–110 km using the Fe Boltzmann technique [*Gelbwachs*, 1994]. The gap between 70 and 80 km exists because neither the Rayleigh nor Fe signal level is sufficient to derive accurate temperatures in this region. For convenience, we name the altitude ranges of 30–70 km and 80–110 km and their subregions as the Rayleigh and Fe regions, respectively, following *Fong et al*. [2014].

The data used in this study were collected during three Antarctic winter seasons (2011 to 2013) when the solar elevation was low ($<3°$). Such low background leads to high-quality temperature measurements. We further screen the data and remove outliers that have low signal-to-noise ratios (SNRs), usually due to clouds. The raw lidar data of photon counts were recorded with resolutions of 1 min and 48 m. In the current study, we use the temperature resolution of 1 h × 1 km in the Rayleigh region in order to reduce the photon

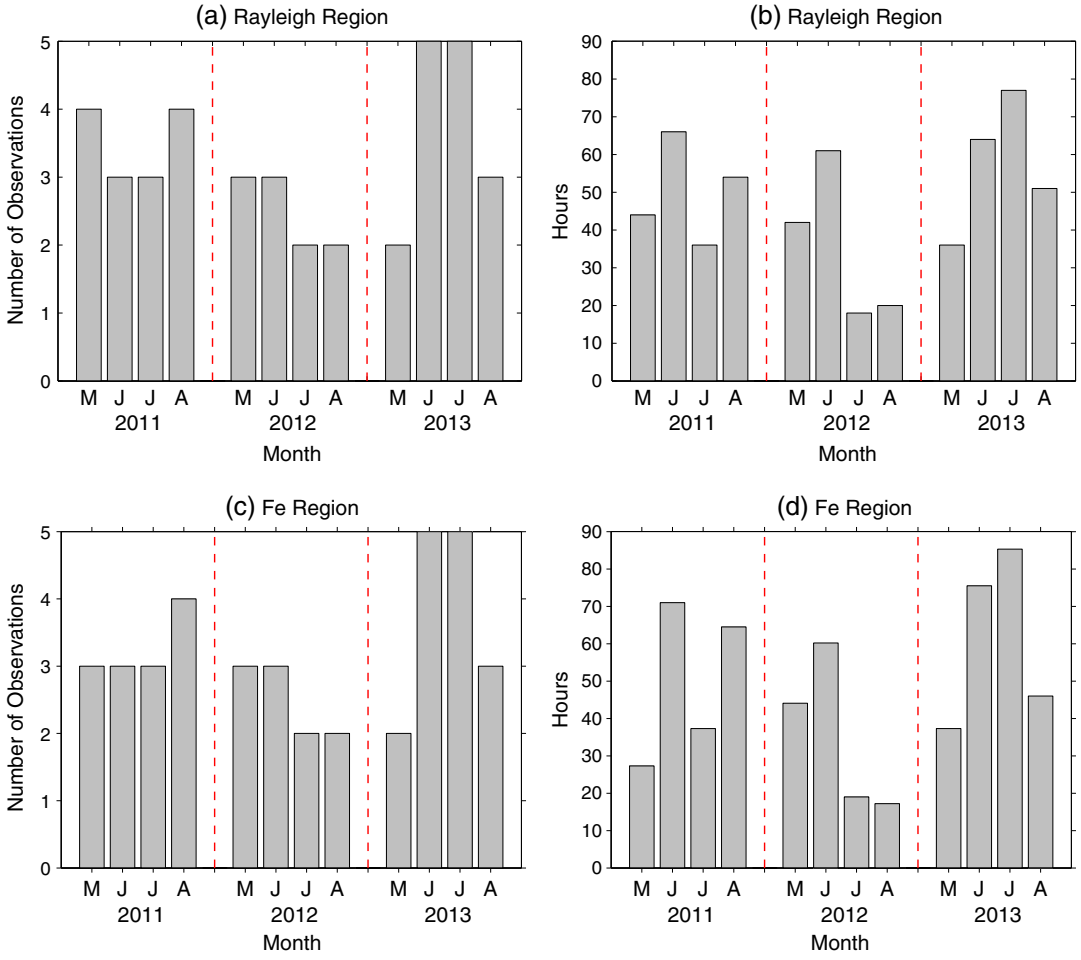

Figure 1. (a) Numbers of observations and (b) total hours in the winter months of May (M), June (J), July (J), and August (A) from 2011 to 2013 in the Rayleigh region. (c) and (d) Same as Figures 1a and 1b, respectively but for the Fe region. Each year is separated by red dashed lines. Only observations longer than 6 h are selected.

noise level, which means that GWs with periods shorter than 2 h and vertical wavelengths shorter than 2 km are not included in the derived GW-E_p. We choose the altitude range of 35–65 km where the SNR is sufficient to calculate the potential energy density. Under the resolution of 1 h × 1 km in the Rayleigh region, typical measurement uncertainties of single temperature profiles increase from 0.2–0.3 K to about 1 K in the altitude ranges of 35–55 km and vary between 1 and 5 K in the altitude range of 55–65 km. The original temperatures in the Fe region are derived at a resolution of 0.25 h × 0.5 km. Under this resolution, the shortest wave period being resolved is 0.5 h and the shortest wavelength is 1 km. In this paper, the GW-E_p and wave number spectra in the Fe region are derived at both the original resolution (0.25 h × 0.5 km) and the resolution of 1 h × 1 km in order to compare with the Rayleigh part and to study the contributions from different wave spectra designated by different data resolutions. At the reduced resolution of 1 h × 1 km, temperature uncertainties are less than 1 K in 81–100 km but vary between 1 and 5 K in the range of 100–105 km.

Only episodes longer than 6 h are selected in this study for the purpose of (1) retrieving more representative background temperature for individual observations and (2) retaining a sufficient number of observations. Here we define one single lidar run as one episode. The data distribution for the three years is illustrated in Figure 1. The total number of observations and total hours are 39 and 569 h for the Rayleigh region, and 38 and 585 h for the Fe region, respectively. Without considering July and August 2012 when the data amount are less than those in other months, the average hours within 1 month are 53.1 and 54.9 h in the Rayleigh and Fe regions, respectively. If considering July and August 2012, the corresponding hours are 47.4 h for the Rayleigh region and 48.8 h for the Fe region, respectively.

3. Potential Energy Densities

Temperature perturbations are related to the vertical displacement of an air parcel from its equilibrium position and can be used as a measure of the potential energy of the waves giving rise to such perturbations. The potential energy density per unit mass E_{pm} and energy density per unit volume E_{pv} are calculated as follows [*Wilson et al.*, 1991a; *Yamashita et al.*, 2009]:

$$E_{pm}(z) = \frac{1}{2}\left(\frac{g}{N_0(z)}\right)^2 \overline{\left(\frac{T'(z)}{T_0(z)}\right)^2} \tag{1}$$

$$E_{pv}(z) = \rho_0(z)E_{pm}(z) = \frac{\rho_0(z)}{2}\left(\frac{g}{N_0(z)}\right)^2 \overline{\left(\frac{T'(z)}{T_0(z)}\right)^2} \tag{2}$$

where T_0 is the monthly mean background temperature and T' is the temperature perturbation for each observational episode. The parameter ρ_0 is the background atmospheric density obtained from the MSIS-00 [*Picone et al.*, 2002]. The parameter g is the gravitational acceleration and we use 9.6 m s^{-2} in the Rayleigh region and 9.5 m s^{-2} in the Fe region, respectively. Overbars denote averaging in the time domain for an individual episode.

Due to strong IGWs, the episode mean temperature contains the residual of IGWs if the episode duration is not an integer number of wave periods; thus, it cannot accurately represent the background temperature. We therefore use the monthly mean temperature (T_0) in equations (1) and (2) to remove the IGW effects on the background temperature more efficiently. The temperature perturbations for each episode (T'), however, are derived by subtracting episode mean temperature instead of the monthly mean value (more detailed description is given in section 3.2). The monthly mean Brunt-Väisälä frequency of background atmosphere is derived from the monthly mean temperature as follows:

$$N_0^2(z) = \frac{g(z)}{T_0(z)}\left[\frac{dT_0(z)}{dz} + \frac{g}{C_p}\right] \tag{3}$$

where C_p (1005 J kg^{-1} K^{-1}) is the dry air specific heat at constant pressure. Before we calculate E_{pm} and E_{pv}, the vertical profile of the monthly mean N_0^2 is Hamming smoothed with a full window width of 5 km to remove small-scale fluctuations. The second term in equation (3) is the dry adiabatic lapse rate of the atmosphere and is around 9.8 K/km. The background atmosphere is considered unstable where $N_0^2 < 0$, i.e., the temperature decreases with altitude faster than 9.8 K/km. To calculate the potential energy density of each episode, we need to derive the monthly mean temperature (T_0), Brunt-Väisälä frequency (N_0^2), and episode temperature perturbation (T').

3.1. Monthly and Winter Mean Temperature and Brunt-Väisälä Frequency

We first calculate the episode mean temperature by averaging temperatures at each altitude. Since the episode lengths vary considerably between 6 and 48 h, they introduce different weightings when estimating the mean quantities and standard deviations. Therefore, the weighted monthly mean temperature (T_0) is derived as

$$T_0(z) = \frac{\sum_{i=1}^{n} w_i T_{i0}(z)}{\sum_{i=1}^{n} w_i}, \tag{4}$$

where $T_{i0}(z)$ is the episode mean temperature and w_i is the episode length with a unit of h. The parameter n is the total number of episodes within each month. Similarly, we derive the winter mean temperature $T_0^*(z)$ by computing the weighted average of the episode mean temperatures within one winter:

$$T_0^*(z) = \frac{\sum_{i=1}^{n^*} w_i T_{i0}(z)}{\sum_{i=1}^{n^*} w_i}, \tag{5}$$

where n^* is the total number of episodes within each winter. The weighted standard deviation of the episode mean temperatures in one winter is calculated as

$$\sigma_T(z) = \sqrt{\frac{\sum_{i=1}^{n^*}\left[w_i\left(T_{i0}(z) - T_0^*(z)\right)^2\right]}{\left(\sum_{i=1}^{n^*} w_i\right)}} \tag{6}$$

The winter mean $N_0^{2^*}(z)$ is derived from the winter mean temperature profile following equation (3) except that the monthly mean temperature is replaced by the winter mean. The same Hamming window smoothing as applied for the monthly mean $N_0^2(z)$ is used for the winter mean $N_0^{2^*}(z)$.

The monthly and winter mean temperatures and Brunt-Väisälä frequencies are shown in Figure 2. The error bars are the weighted standard deviations of the episode mean temperatures in each winter, which represent geophysical variability. According to the winter mean temperature profiles, the mesopause is near 98 km, which is about 2 km lower than that reported at the South Pole [*Pan et al.*, 2002; *Pan and Gardner*, 2003]. The stratopause is near 52 km, a few kilometers lower than the South Pole result [*Pan et al.*, 2002]. The three winter mean temperatures averaged vertically in the Rayleigh (35–65 km) and Fe (81–105 km) regions are listed in Table 1, respectively. The corresponding scale heights of the atmospheric density are calculated as

$$H = \frac{k_B \overline{T_0^*}}{Mg} \tag{7}$$

where k_B is the Boltzmann constant and M is the mean molecular mass. $\overline{T_0^*}$ is the vertically averaged winter mean temperature in the Rayleigh or Fe region. H values provide important information to examine wave energy dissipation.

There is an interannual variability of the background temperatures. The vertically averaged winter mean temperature appears to be colder in 2012 than in 2011 and 2013 as illustrated in Table 1. The winter mean mesopause temperature in 2012 is about 180 K which is ~10 K colder than the other two years. The stratopause temperature is also about 3–4 K colder in 2012 than in 2011 and 2013. It should be noted that the distinct data samplings in the three years may introduce biases to the estimations of winter mean temperatures; thus, more observations from later years will be collected to examine the statistical significance of this interannual variability.

The monthly mean temperatures are higher in July and August than in May and June in the stratosphere, while, in the mesosphere, the coldest temperature is found in July except for 2013. The coldest mesopause temperature is also found in July at the South Pole [*Pan et al.*, 2002]. According to equation (3), a negative temperature gradient ($\frac{dT_0}{dz} < 0$) will result in smaller or even negative N_0^2, corresponding to a less stable or even unstable environment as opposed to a positive temperature gradient. Since the background temperature decreases with altitude in the mesosphere yet increases in the stratosphere and thermosphere, the mean N_0^2 is generally smaller in the mesosphere than in the latter two regions. Minimum winter mean $N_0^{2^*}(z)$ likely occurs near 60–80 km with a value of ~$3 \times 10^{-4}\,s^{-2}$ (Figure 2, right column).

3.2. Derivation of T'

The temperature perturbations for each episode (T') are obtained by first subtracting the episode mean temperature from the initial temperature measurements. Then a high-pass filter with a cutoff frequency at 10 h is further applied in order to suppress long-period waves, such as planetary waves that are dominant in the stratosphere at McMurdo [*Lu et al.*, 2013] and thermal tides. The 10 h cutoff frequency is selected in order to fully include the effects of the strong IGWs, which have periods of 4–9 h observed at McMurdo [*Chen et al.*, 2013]. According to forward sensitivity modeling results (not shown here), this method can sufficiently remove waves with periods longer than 10 h, including planetary waves and tides that have long vertical wavelengths (λ_z). Thus, the remaining contributions are mainly due to GWs. However, this method cannot remove GWs with long λ_z, as long as wave periods are shorter than 10 h. In order to compare GW-E_p with and without including the long-λ_z GWs, we calculate them respectively with and without a vertical high-pass

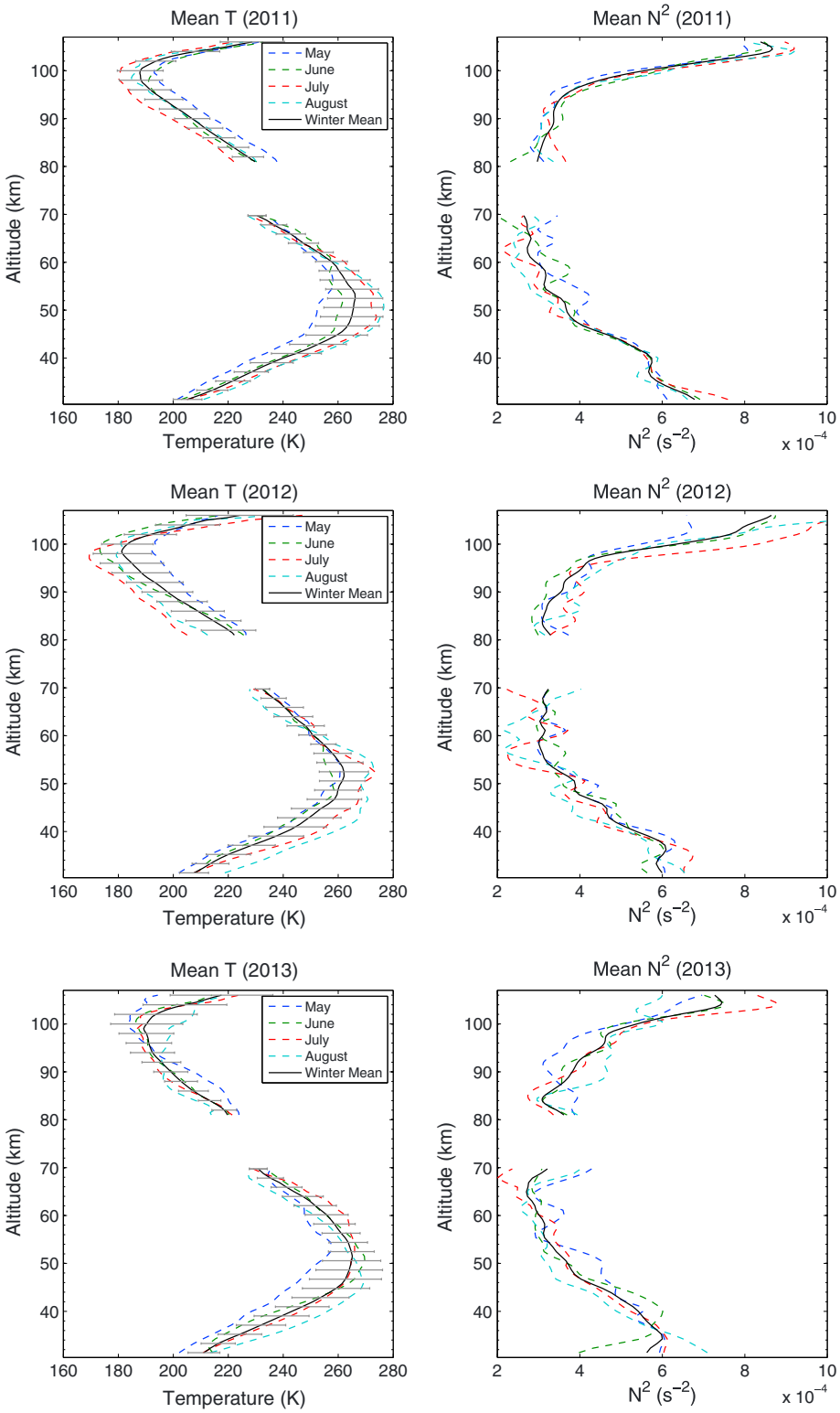

Figure 2. Weighted monthly (color dashed lines) and winter (black solid lines) mean (left) temperatures and (right) N_0^2. The error bars (left) represent the weighted standard deviations of the episode mean temperatures in each winter.

Table 1. Vertically Averaged Winter Mean Temperatures $\overline{T_0^*}$ and Corresponding Atmospheric Scale Heights H in the Fe and Rayleigh Regions, Respectively

	Fe Region (81–105 km)		Rayleigh Region (35–65 km)	
Year	$\overline{T_0^*}$ (K)	H (km)	$\overline{T_0^*}$ (K)	H (km)
2011	205.0	6.19	253.4	7.55
2012	198.2	5.99	249.8	7.44
2013	200.3	6.05	253.4	7.54
Mean	201.2	6.09	252.2	7.51

filtering after the temperature perturbations are obtained in the time domain. The cutoff vertical wavelength is chosen to be 25 km, close to the window width (~25 km) of the Fe region.

The forward modeling tests also indicate that after temperature perturbations are derived in the time domain, the methods of subtracting vertical mean or linear detrending that were conventionally used to suppress long-λ_z waves [*Gardner et al.*, 1998; *Hu et al.*, 2002; *Lu et al.*, 2009] will introduce an artificial wave structure to GW-E_p in our case (not shown here). Therefore, these methods that may be appropriate for the purposes of previous studies are not applied here. As the window width (~25 km in the Fe region) is comparable to but is not the integer number of the vertical wavelength of an IGW (~20 km), the vertical mean of wave-induced temperature perturbation includes a portion of the wave itself. As one IGW or several IGWs dominate, this vertical mean changes with time periodically with the same period as the IGW, which frequently occurs at McMurdo. At an altitude where the time series of the vertical mean temperature is in phase (out of phase) with the wave-induced temperature perturbation, subtracting vertical mean will artificially decrease (increase) GW-E_p. Consequently, GW-E_ps are artificially elevated at some altitudes while suppressed at others, introducing an unrealistic wave structure of GW-E_p. Linear detrending in the vertical domain induces even larger biases since the linear fitting of temperature perturbation can contain a larger portion of the wave itself.

3.3. E_{pm} and E_{pv} Results

After the relative temperature perturbations (T'/T_0) for each episode are obtained, we compute the variances of the relative temperature perturbations over the time domain to obtain E_{pm} and E_{pv} for this episode following equations (1) and (2). The weighted mean and standard deviations of potential energy densities are computed similarly to what we applied for temperature except we replace the temperature in equations (4)–(6) with E_{pm} and E_{pv}.

For conservative gravity waves, E_{pv} should remain constant with altitude while due to the exponential decrease of atmospheric density, E_{pm} increases exponentially with the scale height of the atmospheric density (H). When wave dissipation occurs, E_{pv} decreases with altitude and E_{pm} decreases or increases more slowly than the rate of H. We define the scale heights H_{pm} and H_{pv} to respectively quantify the increasing rate of E_{pm} and the decreasing rate of E_{pv} with altitude:

$$E_{pm}(z) = E_{pm}(z_0)e^{\left(\frac{z-z_0}{H_{pm}}\right)} \tag{8}$$

$$E_{pv}(z) = E_{pv}(z_0)e^{\left(-\frac{z-z_0}{H_{pv}}\right)} \tag{9}$$

The scale heights can then be determined as the ratios of the linear fitting with forms of

$$\ln\left[E_{pm}(z)\right] - \ln\left[E_{pm}(z_0)\right] = (z - z_0)/H_{pm} \tag{10}$$

$$\ln\left[E_{pv}(z)\right] - \ln\left[E_{pv}(z_0)\right] = (z_0 - z)/H_{pv} \tag{11}$$

where H_{pm} and H_{pv} can be used to describe the dissipation rates of the potential energy densities. A larger positive H_{pm} than H means that E_{pm} grows with altitude more slowly than freely propagating waves, thus indicative of more severe dissipation than smaller positive values. H_{pv} denotes the vertical distance over which E_{pv} decreases to its $1/e$. Thus, smaller H_{pv} implies that waves dissipate faster with altitude than larger H_{pv}.

Plotted in Figure 3 are the winter-mean E_{pm} and E_{pv} without filtering in the vertical domain. Error bars represent the uncertainties propagating from raw temperature measurements. We first calculate the uncertainties of temperature perturbations (T') and track the error propagations to E_{pm} and E_{pv} following equations (1) and (2). The dominant waves contributing to the potential energy densities are those with periods

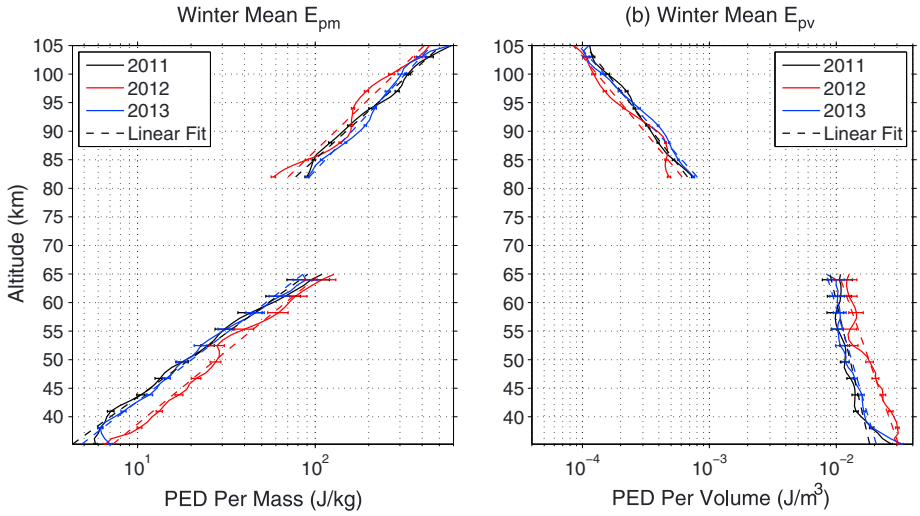

Figure 3. Weighted winter mean potential energy densities (a) per unit mass and (b) per unit volume for the data resolution of 1 h × 1 km. Dashed lines are the linear fittings following equations (10) and (11). Error bars represent uncertainties originating from raw temperature measurements.

between 2 and 10 h, presumably IGWs. The weighted winter mean E_{pm} increases exponentially from several J/kg around 35 km to ~80–120 J/kg near 65 km. According to the relation described in equation (10), the scale height H_{pm} is linearly fitted based on the winter mean E_{pm} and is listed in Table 2. The mean scale height of the three years is about 10.4 km, which is larger than that of the freely propagating wave (7.51 km in the altitude range of 35–65 km), suggesting that wave energy is dissipated in the Rayleigh region. *Wilson et al.* [1991b] also found that the scale height of E_{pm} is generally larger than 10 km using Rayleigh lidar measurements, which is similar to our results. E_{pm} increases from near 100 J/kg to 440–570 J/kg in the Fe region (81–105 km), which also indicates energy dissipation given the scale height of E_{pm} (Table 2). H_{pm}s are comparable in the three years and the mean value is about 13.2 km, which is about twice as large as that for a freely propagating wave (~6.09 km). The relative magnitudes of E_{pm} at 65 km are comparable or larger than the magnitudes at 81 km, suggestive of severe dissipation in between. This point will be further discussed in section 5.

Figure 3b illustrates the vertical variations of the weighted winter mean E_{pv} for the three years. The scale heights of E_{pv} are computed and listed in Table 3. The estimations of H_{pv} reveal that E_{pv} decreases to its 1/*e* by ~11.6 km in the Fe region and by ~33.9 km in the Rayleigh region (Table 3), suggestive of more severe wave dissipation in the Fe region. E_{pv} has decreased by 1 order of magnitude in the Fe region. This is not the first time that the different scale heights and dissipating rates are observed in different altitude ranges using lidar observations. *Rauthe et al.* [2008] also showed larger dissipating rates of E_{pv} above ~80 km at 54°N, and *Mzé et al.* [2014] showed larger dissipating rates above ~70 km at 44°N. Overall, from 35 to 105 km, E_{pv} has decreased by about 2 orders of magnitude at McMurdo, indicating a substantial loss of energy as waves propagate upward.

Table 2. Scale Heights (H_{pm}) of the Winter Mean E_{pm} in the Fe (81–105 km) and Rayleigh (35–65 km) Regions

Region	Resolution	Vertical Filter	2011	2012	2013
Fe	(1 h, 1 km)	No	12.2 ± 0.4[a]	13.0 ± 0.8	14.5 ± 0.6
		Yes[b]	14.2 ± 1.0	13.0 ± 1.0	15.6 ± 1.0
	(0.25 h, 0.5 km)	No	11.8 ± 0.3	13.1 ± 0.6	12.2 ± 0.3
		Yes	15.3 ± 0.6	12.0 ± 0.4	13.2 ± 0.4
Rayleigh	(1 h, 1 km)	No	9.8 ± 0.3	11.1 ± 0.4	10.4 ± 0.3
		Yes	12.2 ± 0.3	13.6 ± 0.5	12.8 ± 0.4

[a]The uncertainties of the linear fitting coefficients are also provided.
[b]A high-pass filter with a cutoff frequency of 25 km is applied in the vertical domain.

Table 3. Scale Height (H_{pv})[a] of the Weighted Winter Mean E_{pv}

Region	Height Range (km)	Resolution	2011	2012	2013
Fe	81–105	(1 h, 1 km)	12.4 ± 0.4[b]	11.7 ± 0.7	10.7 ± 0.4
		(0.25 h, 0.5 km)	12.8 ± 0.2	11.6 ± 0.4	12.4 ± 0.3
Rayleigh	35–65	(1 h, 1 km)	41.3 ± 5.0	27.5 ± 2.3	32.9 ± 3.4

[a] H_{pv} represents the vertical distance over which E_{pv} decreases to its 1/*e*.
[b] The uncertainties of the linear fitting coefficients are also provided.

After we apply the high-pass filtering with a cutoff wavelength at 25 km to the vertical profiles of temperature perturbations, GWs with vertical wavelength longer than 25 km are substantially suppressed compared with the unfiltered results of Figure 3. This results in decreases in E_{pm} and E_{pv}, as illustrated by Figure 4. The maximum values of E_{pm} decrease to ~50–70 J/kg in the Rayleigh region and to ~270–370 J/kg in the Fe region, respectively. On average, E_{pm} in both regions has decreased by a factor of 1.5–2 after the vertical filtering is applied. The uncertainties of E_{pm} after vertical filtering decrease to ~80% compared with unfiltered results. They are also plotted in Figure 4 as error bars. Using the temperature measurements from the Rayleigh lidar at Davis (69°S), Antarctica, *Alexander et al*. [2011a] analyzed the E_{pm} contributed from GWs with periods $\tau > 2$ h and vertical wavelengths $4 < \lambda_z < 20$ km. The orders of the magnitudes of E_{pm} at Davis are quite comparable to our results with vertical filtering [see *Alexander et al*., 2011a, Figure 8b]. The scale heights of E_{pm} with the vertical filtering are also calculated and listed in Table 2. At the resolution of 1 h × 1 km, the mean scale heights of E_{pm} in the Rayleigh and Fe regions are 12.9 and 14.3 km, respectively, which are slightly larger than the data without the vertical filtering (i.e., 10.4 and 13.2 km). Since larger H_{pm} corresponds to more dissipation, it indicates that GWs with $\lambda_z < 25$ km experience slightly higher dissipation than $\lambda_z > 25$ km.

Both Figures 3 and 4 reveal that the winter mean potential energy density is larger in 2012 than in 2011 and 2013 below ~60 km, while the opposite is true in the MLT region, which implies that above 60 km, more wave dissipation occurs in 2012 than the other two years for the data ensemble used in this study. The year-to-year differences are not within the uncertainties in most altitudes except for the upper boundaries of the Rayleigh and Fe regions, indicating that the interannual variability is significant statistically. We speculate that such variability may be related to changes in background winds and temperature, as we have already observed colder winter mean temperatures in 2012 than in the other two years. Further investigations are required to draw conclusions on the mechanisms for such interannual variability. Except for Figure 4, the results in Figures 3–11 are obtained from the temperature perturbations without the vertical filtering.

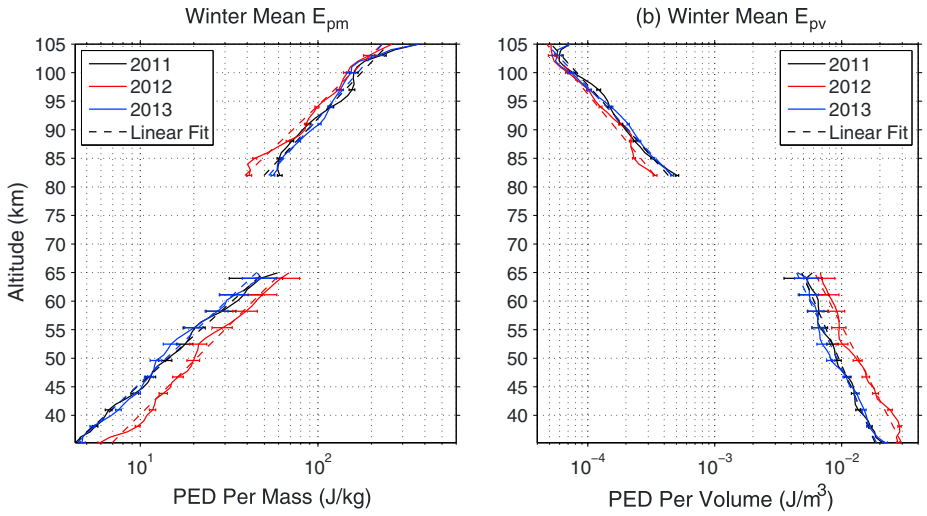

Figure 4. The same as Figure 3 but for the vertical-filtered data with a cutoff frequency at 25 km.

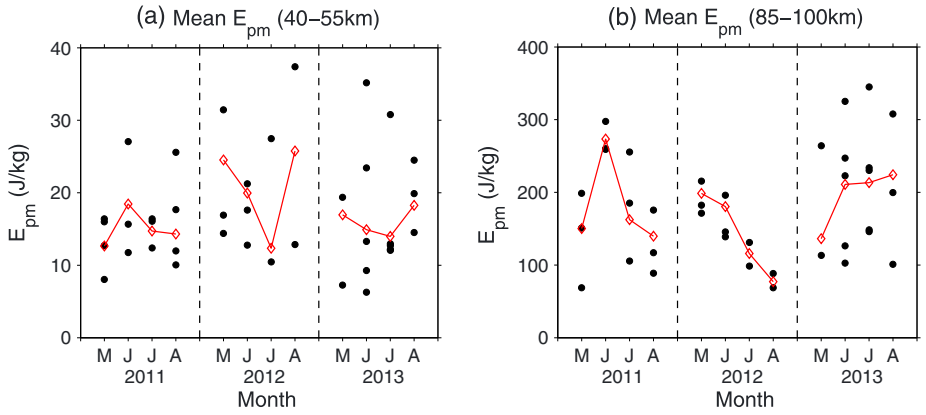

Figure 5. Mean E_{pm} averaged in the altitude region of (a) 40–55 km and (b) 85–100 km for each lidar episode, respectively. The red line is the weighted mean E_{pm} in the month of May (M), June (J), July (J), and August (A) from the year 2011 to 2013. Each year is separated by black dashed lines. The data resolution of 1 h × 1 km is used for the calculation.

Figure 5 shows the episode E_{pm} averaged in the Rayleigh (40–55 km) and Fe (85–100 km) regions using the data resolution of 1 h × 1 km, respectively. These two altitude ranges are chosen due to the relatively small uncertainties. The variability of the mean E_{pm} from one lidar episode to another is large, and the large variability is actually insensitive to the selection of altitude ranges. The maximum and minimum E_{pm} can differ by more than 5 times. The weighted mean and standard deviation of the vertically averaged E_{pm} in the region of 40–55 km for the three years are ~17.2 and 7.2 J/kg, respectively. Their counterparts in the Fe region are ~193.7 and 72.5 J/kg. The large variability of E_{pm} indicates that the strengths of the gravity waves vary considerably for different episodes. This implies that wave sources and/or the physical processes affecting the wave propagation and dissipation such as filtering, reflection, or ducting, are playing different roles from one episode to another.

Using higher temporal and vertical resolutions would include more waves with higher frequencies and smaller wavelengths than the case with lower resolutions. The consequent observational filtering effects are different on the phenomena of interest and deserve investigation [*Alexander*, 1998]. As mentioned in section 2, we also calculate E_{pm} with the original resolution of 0.25 h × 0.5 km for the Fe region and the winter mean results are shown in Figure 6a. At this resolution, the contributing waves are mainly those with periods longer than 0.5 h and vertical wavelengths longer than 1 km. Similar vertical structure of E_{pm} is observed for the original resolution except that the magnitude is increased as expected. This similarity does highlight the fact that these small waves can be observed by the lidar observations, which provide opportunities for

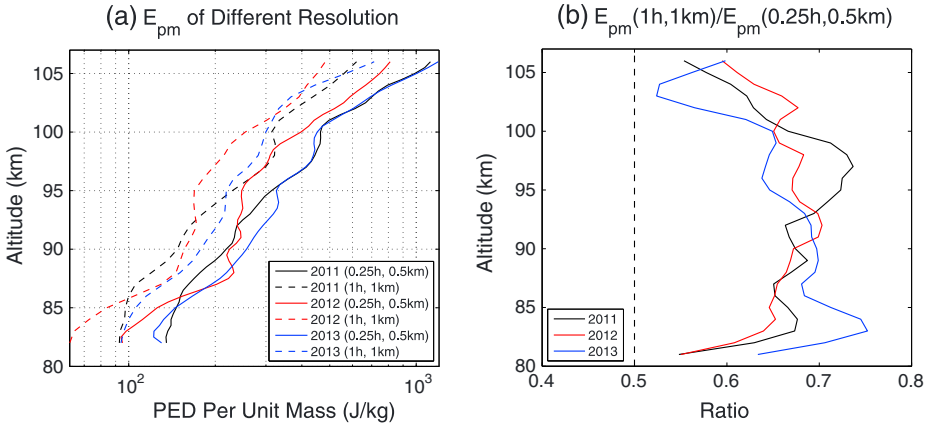

Figure 6. (a) Weighted winter mean potential energy densities per unit mass for the resolutions of (0.25 h, 0.5 km) and (1 h, 1 km), respectively; (b) Ratios of the E_{pm} computed with these two resolutions.

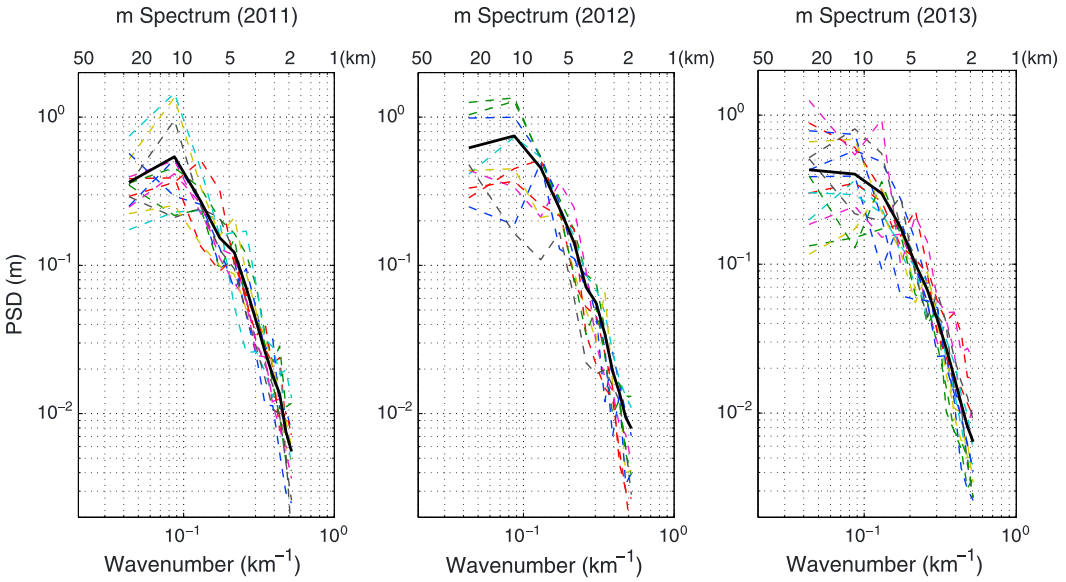

Figure 7. Mean vertical wave number spectra for individual lidar episodes (colored dashed lines) and for one winter (black solid lines) in the Rayleigh region (35–60 km). Vertical wavelengths at 50, 20, 10, 5, 2, and 1 km are denoted at the upper *x* axes.

further work. The scale heights of E_{pm} and E_{pv} for the original resolution are also calculated and listed in Tables 2 and 3. They are quite comparable with the scale heights for the resolution of 1 h × 1 km, which imply that the mechanisms for the wave dissipation likely have similar effects upon the two different wave spectra designated by the two resolutions used in this study. The ratio of E_{pm} calculated from the low resolution to that from the high resolution is shown in Figure 6b. The waves with periods longer than 2 h and vertical wavelengths longer than 2 km contain 55–75% of the total potential energy of the waves with periods longer than 0.5 h and vertical wavelengths longer than 1 km. From 85 to 100 km, the percentage can reach 65–75%. In other words, the E_{pm} of 0.5–2 h waves consist of ~25–45% of the total E_{pm} for 0.5–10 h waves, which indicates that the short-period waves contribute a substantial portion to the total E_{pm}.

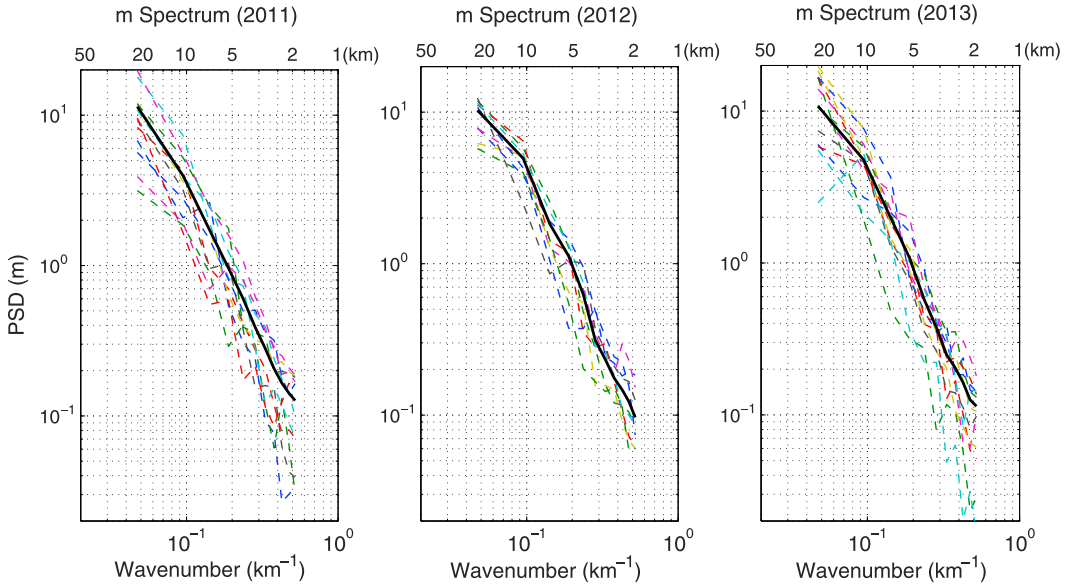

Figure 8. Similar to Figure 7 but for the Fe region.

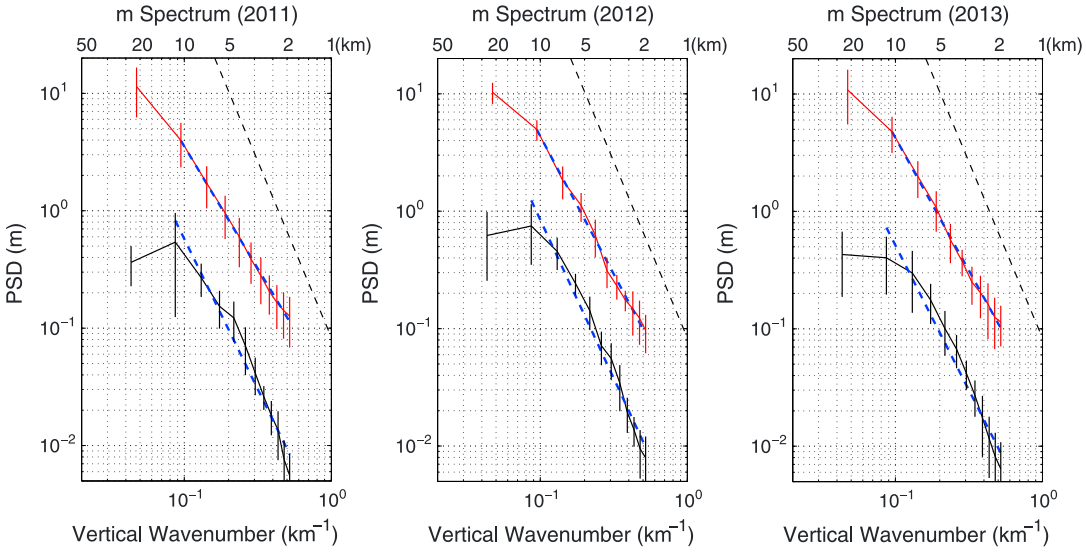

Figure 9. Weighted winter mean vertical wave number spectra in the Rayleigh (black) and Fe (red) regions. Blue dashed lines are the linear fittings of the power law shapes in the range of ~2–10 km. Black dashed lines only provide a reference for the slope of −3 while their PSD values do not serve for any comparison purposes. The error bars denote the weighted standard deviations of the episode PSDs in each winter.

4. Vertical Wave Number Spectra

Similar to *Dewan and Grossbard* [2000], the power spectral density (PSD) is derived using the Discrete Fourier Transform (DFT) as

$$F(m_k) = \frac{\Delta z |f(m_k)|^2}{N} = \frac{\Delta z}{N}\left|\sum_{n=1}^{N} x(z_n) e^{-\frac{2\pi(n-1)(k-1)}{N} i}\right|^2 \quad (12)$$

where m_k is the k^{th} wave number and $f(m_k)$ denotes its DFT value. Δz is the vertical interval of the data set and N is the total points of a single vertical profile. The parameter $x(z_n)$ is the relative temperature perturbation (T'/T_0) at altitude z_n. With the resolution of 1 h × 1 km in the Rayleigh region and 0.25 h × 0.5 km in the Fe region, there are no apparent white noise floors at the high wave number end of the spectra. Thus, the fitting of the spectral slope is made without subtracting the noise floors, similar to *Gardner et al.* [1989] and *Senft and Gardner* [1991].

After the relative temperature perturbations for each episode are obtained as described in section 3.2, we calculate the PSD for each vertical profile of the relative temperature perturbation and then average all the PSDs in one lidar episode to derive the episode mean. We select the altitude range of 35–60 km for the Rayleigh region and 81–105 km for the Fe region for the PSD calculation, respectively. When we estimate the slopes of wave number spectra, we focus on the range of $2 < \lambda_z < 10$ km. Thus, the vertical filtering with a cutoff frequency at 25 km has a minor effect on the spectral slopes and the data without the vertical filtering are used in this section. In order to better compare the PSDs in these two regions, the same resolution of 1 h × 1 km is

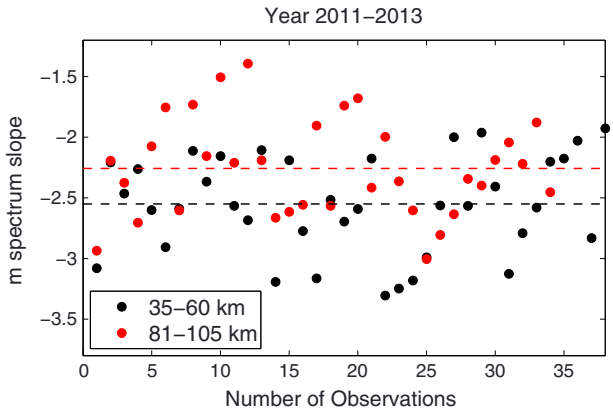

Figure 10. Slopes of the vertical wave number spectra for individual episodes (dots). Dashed lines mark their weighted means. Black color is for the Rayleigh region and red color is for the Fe region, respectively.

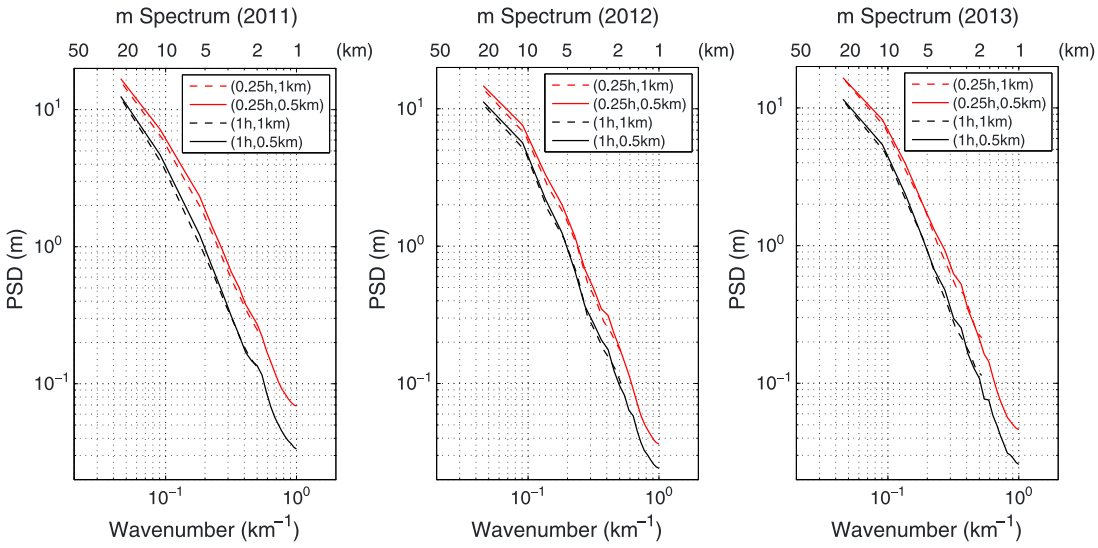

Figure 11. The vertical wave number spectra under different resolutions in the Fe region.

used in Figures 6–9. The weighted winter mean and standard deviation of the wave number spectra are calculated similarly to those of the background temperature.

Figure 7 shows that the maximum PSD is on the order of 10^0 $(1/m)^{-1}$ in the Rayleigh region which is comparable to the studies in *Beatty et al*. [1992] and *Senft et al*. [1993], both calculating the PSDs of the atmospheric relative densities using the lidar data at Arecibo. In their studies, a low-pass filter with cutoff frequency of 2π/1 h was applied for the Rayleigh data which limited the observed period to be approximately 100 min or longer. Their observations were nighttime only which ranged from several hours to 10–12 h. Our study therefore focuses on a similar portion of the wave spectrum (mainly 2–10 h), although it is not exactly the same as *Beatty et al*. [1992] and *Senft et al*. [1993]. The characteristic vertical wave number m^* denoted as the turning point of the spectrum is around 0.087 km^{-1} in 2011 and 2012, corresponding to a characteristic vertical wavelength (λ_z^*) of ~11.5 km. For vertical wave numbers smaller than 0.1 km^{-1} (vertical wavelengths larger than 10 km), the PSDs have a large variability (can be up to an order of magnitude) from one episode to another. We have named this case-to-case variability. This variability may arise from the different source spectra or from the differences in critical level filtering.

Using data with the same resolution of 1 h × 1 km, the PSD in the Fe region (Figure 8) is about 1 order of magnitude larger than that in the Rayleigh region. In addition to the increased magnitude, the spectral shape in the Fe region is also distinct. Instead of having a characteristic wave number m^*, the PSD in the Fe region is monotonically growing for the increasing vertical wavelength so the characteristic wavelength λ_z^* is no shorter than 20 km. Another difference is that instead of showing large case-to-case variability for wave numbers smaller than 0.1 km^{-1} in the Rayleigh region, the relative variability is more uniformly distributed with respect to different vertical wave numbers in the Fe region. Presumably, the wave spectra would carry more characteristics of the source spectra at places closer to the source (near fields), while at far fields, other factors such as saturation, dissipation, and mean wind filtering may play active roles and smear out the source features. The large case-to-case variability observed in the Rayleigh region, but not in the Fe region may imply that the source region for waves with $\lambda_z >$ ~10 km is closer to the Rayleigh region than the Fe region. This may be consistent with the suggestion in *Chen et al*. [2013] that IGWs at McMurdo are generated around 40 km by the unbalanced flow associated with the polar vortex. The Rayleigh region will also be more affected by sources if waves are generated near the surface.

The winter mean PSDs are replotted in Figure 9 for both regions, superimposed by the linear fittings of the power law shapes. The PSDs in both regions tend to follow the power law for wave numbers larger than ~0.1 km^{-1} ($\lambda_z <$ ~10 km). The spectral slopes are fitted and listed in Table 4. It is seen that the slopes of the vertical wave number spectra in the Rayleigh region are slightly steeper and closer to −3 than in the

Table 4. PSD Slopes Fitted in the Spectral Range of 2–10 km Under Different Resolutions

Altitudes	Resolution	2011	2012	2013
35–60 km	(1 h, 1 km)	-2.56 ± 0.17[a]	-2.70 ± 0.15	-2.47 ± 0.18
81–105 km	(1 h, 1 km)	-2.08 ± 0.03	-2.35 ± 0.07	-2.26 ± 0.04
	(0.25 h, 1 km)	-1.98 ± 0.03	-2.23 ± 0.05	-2.10 ± 0.04
	(1 h, 0.5 km)	-2.18 ± 0.05	-2.39 ± 0.05	-2.33 ± 0.04
	(0.25 h, 0.5 km)	-1.99 ± 0.05	-2.22 ± 0.05	-2.15 ± 0.05

[a]Uncertainties arisen from the linear fitting method.

Fe region. From the Rayleigh to the Fe region, the PSD increases by ~4–10 times in the spectral range of 2–10 km and by more than 10 times for the vertical wavelength near 20 km, indicative of the largest growth for waves with vertical wavelengths of ~20 km. This is supportive of the finding that IGWs are the dominant feature in the observed MLT temperature and usually possess vertical wavelengths around 20 km [*Chen et al*., 2012, 2013, 2014]. The smallest increase of PSDs from the Rayleigh to the Fe region is observed in 2012 while the largest increase is seen in 2013, which is similar to the smallest increase of E_{pm} in 2012.

The spectral slopes for all the episodes in the three winters are also derived and illustrated in Figure 10. The slope values are between −1.9 and −3.3 in the Rayleigh region and between −1.4 and −3.0 in the Fe region. The wide distributions of the spectral slopes are similar to the study of *Senft and Gardner* [1991], which has shown that the slopes of the vertical wave number spectra range between −2.20 and −3.55 using over 60 nights of Na lidar observations at Urbana, Illinois. The weighted mean slope for all the episodes through three winters is about −2.55 in the Rayleigh region with a standard deviation of ~0.36. In the Fe region, the mean slope is about −2.26 and the standard deviation is ~0.38.

The spectral shapes for different resolution data are similar while the magnitudes of the PSD have a stronger dependence on the temporal resolution than the vertical resolution, and as expected, higher temporal resolution includes more waves and corresponds to a larger PSD (Figure 11). The PSD differences between the temporal resolution of 1 and 0.25 h with the same vertical resolution are quantitatively illustrated in Figure 12. We provide the year 2013 as an example as the other two years are similar. Although the absolute increase in PSD from the temporal resolution of 0.25 to 1 h is larger for longer vertical wavelengths, the ratios of the PSDs under different temporal resolutions peak at shorter vertical wavelengths. Due to the power law dependence of PSDs on wave number, the spectral slopes are more affected by the relative increases of PSDs instead of the absolute increases; thus, we illustrate the ratios of PSDs in Figure 12b. For vertical wavelengths longer than 10 km, the increase of PSD after introducing 0.25 h resolution is less than 50%. This implies that gravity waves with periods between 0.5 and 2 h are not dominant in the wave spectrum of long vertical wavelengths ($\lambda_z > 10$ km). However, for vertical wavelengths between 2 and 5 km, if we increase the temporal resolution from 1 to 0.25 h while keeping the vertical resolution the same (either 0.5 or 1 km), the ratios of PSDs under these two different temporal resolutions are larger than 1.8, which indicates that including the gravity waves with periods of 0.5–2 h can increase the total PSD by more than 80%. Although *Beatty et al*. [1992] did not provide the quantitative analyses of the PSD differences and ratios as a function of

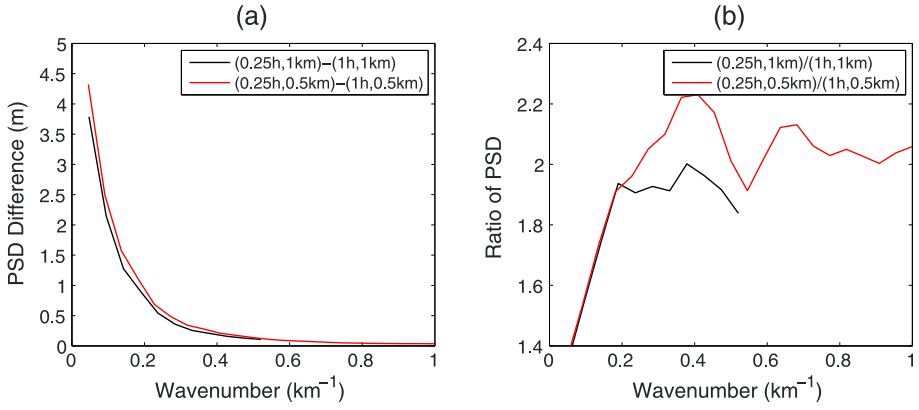

Figure 12. (a) PSD differences and (b) PSD ratios under the same vertical resolution but different temporal resolutions for year 2013. Black line is for the vertical resolution of 1 km and red line is for 0.5 km.

wave number, their qualitative estimation that the magnitude of the spectrum filtered at 1 h^{-1} is about a factor of 2 smaller than that filtered at 5 $(min)^{-1}$ is similar to our findings.

The spectral slopes with different resolutions are listed in Table 4. Although the values are close to each other, a closer inspection shows that the wave number spectra derived with higher temporal resolutions appear to have shallower slopes than the lower temporal resolutions. This suggests that gravity waves with shorter periods increase the PSDs of the shorter wavelengths more efficiently than that of longer wavelengths. This will have an effect of flattening the vertical wave number spectrum. The same feature is also seen in Figure 13 of *Beatty et al*. [1992].

In general, the slope of the wave number spectrum in the MLT at McMurdo appears to be shallower than those reported at middle and low latitudes. For instance, *Beatty et al*. [1992] and *Senft et al*. [1993] reported that the *m* slope is close to −3 in the upper mesosphere at Arecibo (18°N) in the spectral range of 1–10 km; *Yang et al*. [2010] reported a mean value of −3.08 using the Na temperature lidar measurement at São José Dos Campos, Brazil (23°S), in the spectral range of 2–7 km; *Senft and Gardner* [1991] reported a mean slope of −2.90 for the *m* spectrum using the Na lidar observation at Urbana, Illinois (40°N), in the spectral range of 1–10 km. Nevertheless, the *m* slope in the mesosphere at the South Pole was found to be −2.3 in the spectral range of 1.4–10 km in *Collins et al*. [1994], which is more comparable to our measurements at McMurdo (−2.26). The combination of our observation with the previous reports reveals a latitudinal dependence of the spectral slope that tends to become shallower for higher latitudes in the MLT. Such latitudinal dependence has already been identified in the stratosphere using the radiosonde observations [*Allen and Vincent*, 1995; *Pfenninger et al*., 1999].

5. Discussion

For a case study of the potential energy of a single or multiple gravity waves, the decrease of the wave energy with altitude can be caused not only by wave dissipation but also by waves propagating out of the field of view of the lidar or wave properties being shifted outside of the GW spectra that can be observed by the lidar. By the same token, if a wave propagates into the field of view at a certain altitude or its properties are shifted within the detectable GW spectra, it will be manifested as an increase of wave energy above it. In this paper, an assumption has to be made that the effects caused by the waves propagating into or out of the lidar view or their prosperities being shifted into or out of the detectable spectral range, if they exist, should cancel out each other statistically so their effects on GW-E_p are negligible.

It is intriguing that in the gap region of 65–81 km, the dissipation of the wave energy is more severe than the regions below and above for both the vertically filtered and unfiltered data (see Figures 3 and 4). The vertical variations of E_{pm} and E_{pv} also appear to be discontinuous in this region, where the values of E_{pm} barely increase in 2011 and 2013 and even decrease in 2012. E_{pv} also decreases by 1 order of magnitude over only 16 km in the gap. Interestingly, *Preusse et al*. [2006] have also identified a decrease of GW activity at the top of the southern polar vortex (~60 km) using the Sounding of the Atmosphere using Broadband Emission Radiometry (SABER) temperature measurements in August 2003. In their Figure 2, the zonal mean GW temperature amplitudes reveal obvious decreases in the region of 60–80 km at latitudes of ~60–80°S, which is similar to our findings. *Preusse et al*. [2006] argued that a possible mechanism for the decreased GW activity is the enhanced wave breaking on top of the polar jet inferred from numerical simulations. As GWs propagate through and against the polar jet composed of strong eastward zonal mean winds [*Lu et al*., 2013], they are refracted to longer vertical wavelengths, and if they leave the polar jet above ~60 km, the vertical wavelengths become shorter again, and thus, waves become easier to break and experience larger dissipation. In addition to this argument, our analysis hints that the gap region has the smallest $N_0^2(z)$ linked with an increased likelihood of convective instability. This occurs because the background is easier to be forced toward convective instability. We have observed cases of convectively unstable regions in the upper mesosphere using the Fe region data supporting this argument (not shown here). If convective instability occurs, gravity waves will also likely break with energies being lost and converted to turbulence.

Figures 11 and 12 allow us to examine the impact of observational filtering on our measurements. In particular, we can examine how short-period waves impact the PSD. Previous studies have focused on the

impact of observational filtering on satellite data [*Alexander*, 1998; *Alexander et al*., 2008; *Preusse et al*., 2008]. Since the increase of PSD ratios after introducing 0.25 h resolution is smallest at long λ_z, we can infer that the short period waves observed by the lidar also have short λ_z thus short horizontal wavelengths [from *Fritts and Alexander*, 2003, equation (30)]. This combination of vertical and horizontal wavelengths is likely associated with the mountain waves in this region [*Baumgaertner and McDonald*, 2007] with several other papers identifying similar combinations of vertical and horizontal wavelengths connected to mountain waves at high southern latitudes [*Preusse et al*., 2002; *Alexander and Teitelbaum*, 2007]. This is interesting since it suggests that some of these waves, which are supposed to have zero-phase speeds relative to the ground if generated by constant winds blowing over topography, can make their way to the mesosphere in this region. This implication is supported by previous studies. For instance, *Yamashita et al*. [2009] have found that the mountain waves at Rothera (67.5°S), Antarctica, have very little chance of reaching 30–45 km in summer but have much higher probabilities in winter, consistent with significant wind rotations (>90°) in summer while smaller wind rotations in winter in the lower atmosphere. Moreover, according to the measurements by the Upper Atmosphere Research Satellite, zonal mean winds are persistently eastward from the surface to the MLT region in winter including the 4 months investigated in our study [*Swinbank and Ortland*, 2003]; thus, mountain waves are less likely to encounter zero wind lines so have higher likelihood of reaching the MLT region.

The lidar observations of the vertical wave number spectra can be divided into two categories: one is supportive of the linear saturation theory and the other is not. The supportive ones can be found in *Whiteway and Carswell* [1994, 1995], who reported that the spectral slope was close to −3 and the PSDs did not increase with altitude according to the Rayleigh lidar temperature measurements in the high Arctic (80°N). Many other studies [*Wilson et al*., 1991a; *Beatty et al*., 1992; *Senft and Gardner*, 1991; *Senft et al*., 1993; *Yang et al*., 2010; *Alexander et al*., 2011a], however, do not support this theory. Our observation is also not supportive of the linear saturation theory since the spectral slope is not equal to −3 and it has a large case-to-case variability. In addition, the linear saturation theory predicts that the PSD should be proportional to N^4/m^3 for the temperature spectra [*Fritts et al*., 1988; *Beatty et al*., 1992; *Senft et al*., 1993]. In order for the PSD to increase by 1 order of magnitude, N^2 has to increase by at least 3 times from the Rayleigh to the Fe regions, which is not always true if we follow the vertical variation of N^2 with altitude.

It is worthwhile mentioning that there is no definite physical justification to prove that the GWs with spectra following the power law are necessarily saturated in our observations. As shown by the increased PSDs and large day-to-day variability of spectral slopes, we cannot exclude the possibility that the observed wave spectra consist of unsaturated GWs, especially in the Rayleigh region. In fact, Weinstock's diffusive damping theory [*Weinstock*, 1990] suggests that saturation can be influenced by the source spectrum, and when the source energy is dominated by low wave numbers in the troposphere, the mesospheric spectrum will not be saturated at scales as short as a few kilometers. In this case, the magnitude and slope of the spectrum can differ considerably from the predicted saturation values. This potentially occurs at McMurdo since the IGWs are dominant in the mesopause region and are often characterized by low vertical wave numbers [*Chen et al*., 2013].

6. Conclusions

We present a statistical study of the potential energy densities and vertical wave number spectra of GWs using the winter temperature measurements at McMurdo (77.8°S, 166.7°E), Antarctica, from 2011 to 2013. The potential energy density per unit volume (E_{pv}) decreases by 2 orders of magnitude from 35 to 105 km. In the altitude region of 35–65 km (Rayleigh region), the scale height of E_{pv} decrease is ~34 km, while it is ~12 km in the region of 81–105 km (Fe region), suggestive of stronger wave dissipation in the Fe region than in the Rayleigh region. The potential energy density per unit mass (E_{pm}) increases from several to hundreds of J/kg from 35 to 105 km, characterized by a mean scale height (H_{pm}) of ~10.4 km in the Rayleigh region and ~13.2 km in the Fe region, respectively. Therefore, the vertical evolutions of E_{pv} and E_{pm} indicate substantial energy dissipation as gravity waves propagate from the stratosphere to the lower thermosphere. The vertical evolution of the potential energy densities is similar and the corresponding scale heights are comparable in different years; thus, these features are statistically significant. The year-to-year variability shows that 2012 appears to experience more dissipation than 2011 and 2013 above 60 km, which may be

related to the yearly variability of the background conditions. The large case-to-case variability of E_{pm} identified suggests considerable differences in the GW activity between episodes, which are possibly source driven or caused by mean wind filtering.

The spectra of the vertical wave number follow the power law for $\lambda_z < \sim 10$ km. The mean spectral slopes of the vertical wave number in the spectral range of ~2–10 km are -2.55 in the Rayleigh region and -2.26 in the Fe region, respectively. The spectral slope of the Fe region points to the latitudinal dependence with shallower slopes at high latitudes than low and middle latitudes. The case-to-case variability of the spectral slopes is large, implying that in addition to the saturation and dissipation processes, the differences in the source spectra and critical level filtering may be also important in determining the spectral shapes. The characteristic wavelength λ_z^* in the Rayleigh region is about 11.5 km while it increases to $\lambda_z^* > 20$ km in the Fe region. The wave number spectra in the Rayleigh region have a large variability for $\lambda_z > 10$ km, while such variability is not found in the Fe region, which suggests that the Rayleigh region is closer to the wave source than the Fe region. The PSDs in the Fe region are about 1 order of magnitude larger than those in the Rayleigh region. Similar increases of the PSDs from the stratosphere to the mesosphere have also been reported in the studies by *Beatty et al*. [1992] and *Senft et al*. [1993]. However, their studies show that the wave number spectra are steeper (closer to -3) in the mesosphere than those in the stratosphere, which is opposite to our results.

E_{pm} calculated with two different resolutions in the Fe region are compared and higher resolutions contain more waves and thus correspond to larger E_{pm}. The vertical evolution of E_{pm} and its scale height H_{pm} are comparable for both resolutions. The dependence of the spectral magnitude and slope on temporal resolution is also identified, and using higher temporal resolution will increase the PSD and slightly flatten the spectral slope. Including gravity waves with dominant periods between 0.5 and 2 h would increase the PSDs of shorter waves ($2 < \lambda_z < 5$ km) by a factor of 2 while such increase is less than 50% for longer waves ($\lambda_z > 10$ km).

Both the scale heights of potential energy densities and the spectral slopes of the vertical wave number vary considerably from the stratosphere to the MLT. The vertical evolution of the background temperature and winds may be responsible for the differences and variations. Further investigations are needed to explore the physical mechanisms for the vertical evolution of potential energy densities and wave number spectra. E_{pm} shows a severe wave dissipation in the region of 65–81 km, which has also been reported in the previous work of *Preusse et al*. [2006]. Such indication needs further observational support and its dissipation mechanisms also deserve future studies.

Acknowledgments

We are grateful to Chester S. Gardner and David Fritts for valuable discussion on the gravity wave saturation theories, and Anne Smith and Rolando Garcia for helpful discussion on gravity wave potential energy densities. We acknowledge the staff of United States Antarctic Program, McMurdo Station, Antarctica, New Zealand, and Scott Base for their superb support. We offer special thanks to Vladimir Papitashvili of the National Science Foundation and Ed Butler of the Antarctica New Zealand for their encouragement and help in this collaborative research. We thank Wentao Huang, John Smith, Zhangjun Wang, Jian Zhao, and Julie Palais for their contributions and support to the McMurdo lidar campaign. This project was supported by the National Science Foundation (NSF) grants ANT-0839091, PLR-1246405, and AGS-1343106 (CEDAR). The data producing the results of this paper can be requested by communicating with the corresponding authors.

References

Alexander, M. J. (1998), Interpretations of observed climatological patterns in stratospheric gravity wave variance, *J. Geophys. Res.*, *103*(D8), 8627–8640, doi:10.1029/97JD03325.

Alexander, M. J., and A. W. Grimsdell (2013), Seasonal cycle of orographic gravity wave occurrence above small islands in the Southern Hemisphere: Implications for effects on the general circulation, *J. Geophys. Res. Atmos.*, *118*, 11,589–11,599, doi:10.1002/2013JD020526.

Alexander, M. J., and H. Teitelbaum (2007), Observation and analysis of a large amplitude mountain wave event over the Antarctic peninsula, *J. Geophys. Res.*, *112*, D21103, doi:10.1029/2006JD008368.

Alexander, P., A. de la Torre, and P. Llamedo (2008), Interpretation of gravity wave signatures in GPS radio occultations, *J. Geophys. Res.*, *113*, D16117, doi:10.1029/2007JD009390.

Alexander, S. P., A. R. Klekociuk, and D. J. Murphy (2011a), Rayleigh lidar observations of gravity wave activity in the winter upper stratosphere and lower mesosphere above Davis, Antarctica (69°S, 78°E), *J. Geophys. Res.*, *116*, D13109, doi:10.1029/2010JD015164.

Alexander, S. P., A. R. Klekociuk, M. C. Pitts, A. J. McDonald, and A. Arevalo-Torres (2011b), The effect of orographic gravity waves on Antarctic polar stratospheric cloud occurrence and composition, *J. Geophys. Res.*, *116*, D06109, doi:10.1029/2010JD015184.

Allen, S. J., and R. A. Vincent (1995), Gravity wave activity in the lower atmosphere: Seasonal and latitudinal variations, *J. Geophys. Res.*, *100*, 1327–1350, doi:10.1029/94JD02688.

Baumgaertner, A. J. G., and A. J. McDonald (2007), A gravity wave climatology for Antarctica compiled from Challenging Minisatellite Payload/Global Positioning System (CHAMP/GPS) radio occultations, *J. Geophys. Res.*, *112*, D05103, doi:10.1029/2006JD007504.

Beatty, T. J., C. A. Hostetler, and C. S. Gardner (1992), Lidar observations of gravity waves and their spectra near the mesopause and stratopause at Arecibo, *J. Atmos. Sci.*, *49*, 477–496.

Chen, C., X. Chu, Z. Yu, W. Fong, A. J. McDonald, X. Lu, and W. Huang (2012), Lidar and radar investigation of inertia gravity wave intrinsic properties at McMurdo, Antarctica, Proceedings of the 26th International Laser Radar Conference, 1057–1060, Greece, 25–29 June.

Chen, C., X. Chu, A. J. McDonald, S. L. Vadas, Z. Yu, W. Fong, and X. Lu (2013), Inertia gravity waves in Antarctica: A case study using simultaneous lidar and radar measurements at McMurdo/Scott Base (77.8°S, 166.7°E), *J. Geophys. Res. Atmos.*, *118*, 2794–2808, doi:10.1002/jgrd.50318.

Chen, C., X. Chu, W. Fong, A. J. McDonald, P. Pautet, and M. J. Taylor (2014), Mystery of polar inertia-gravity waves: An observational study combining lidar, radar and airglow imager at McMurdo/Scott Base, Abstract 77.8°S, 166.7°E presented at 2014 Fall Meeting, AGU, San Francisco, Calif., 15–19 Dec.

Chu, X., W. Pan, G. Papen, C. S. Gardner, and J. A. Gelbwachs (2002), Fe Boltzmann temperature lidar: Design, error analysis, and first results from the North and South poles, *Appl. Opt.*, *41*, 4400–4410, doi:10.1364/AO.41.004400.

Chu, X., W. Huang, F. Fong, Z. Yu, Z. Wang, J. A. Smith, and C. S. Gardner (2011a), First lidar observations of polar mesospheric clouds and Fe temperatures at McMurdo (77.8°S, 166.7°E), Antarctica, *Geophys. Res. Lett.*, *38*, L16810, doi:10.1029/2011GL048373.

Chu, X., Z. Yu, C. S. Gardner, C. Chen, and W. Fong (2011b), Lidar observations of neutral Fe layers and fast gravity waves in the thermosphere (110–155 km) at McMurdo (77.8°S, 166.7°E), Antarctica, *Geophys. Res. Lett.*, *38*, L23807, doi:10.1029/2011GL050016.

Chu, X., Z. Yu, C. Chen, W. Fong, W. Huang, C. S. Gardner, Z. Wang, B. Roberts, and J. A. Smith (2012), McMurdo lidar campaign: A new look into polar upper atmosphere, in *Proceeding of the 26th International Laser Radar Conference*, pp. 1019–1022, Porto Heli, Greece, 25–29 June.

Collins, R. L., A. Nomura, and C. S. Gardner (1994), Gravity waves in the upper mesosphere over Antarctica: Lidar observations at the South Pole and Syowa, *J. Geophys. Res.*, *99*(D3), 5475–5485, doi:10.1029/93JD03276.

Dewan, E. M., and R. E. Good (1986), Saturation and the "universal" spectrum for vertical profiles of horizontal scalar winds in the atmosphere, *J. Geophys. Res.*, *91*(D2), 2742–2748, doi:10.1029/JD091iD02p02742.

Dewan, E. M., and N. Grossbard (2000), Power spectral artifacts in published balloon data and implications regarding saturated gravity wave theories, *J. Geophys. Res.*, *105*(D4), 4667–4683, doi:10.1029/1999JD901108.

Fong, W., X. Lu, X. Chu, T. J. Fuller-Rowell, Z. Yu, B. R. Roberts, C. Chen, C. S. Gardner, and A. J. McDonald (2014), Winter temperature tides from 30 to 110 km at McMurdo (77.8°S, 166.7°E), Antarctica: Lidar observations and comparisons with WAM, *J. Geophys. Res. Atmos.*, *119*, 2846–2863, doi:10.1002/2013JD020784.

Fritts, D. C., and M. J. Alexander (2003), Gravity wave dynamics and effects in the middle atmosphere, *Rev. Geophys.*, *41*(1), 1003, doi:10.1029/2001RG000106.

Fritts, D. C., T. Tsuda, T. Sato, S. Fukao, and S. Kato (1988), Observational evidence of a saturated gravity wave spectrum in the troposphere and lower stratosphere, *J. Atmos. Sci.*, *45*, 1741–1759.

Gao, X., J. W. Meriwether, V. B. Wickwar, T. D. Wilkerson, and S. Collins (1998), Rayleigh lidar measurements of the temporal frequency and vertical wave number spectra in the mesosphere over the Rocky Mountain region, *J. Geophys. Res.*, *103*(D6), 6405–6416, doi:10.1029/97JD03073.

Garcia, R. R., and S. Solomon (1985), The effect of breaking gravity waves on the dynamics and chemical composition of the mesosphere and lower thermosphere, *J. Geophys. Res.*, *90*(D2), 3850–3868, doi:10.1029/JD090iD02p03850.

Gardner, C. S. (1994), Diffusive filtering theory of gravity wave spectra in the atmosphere, *J. Geophys. Res.*, *99*, 20,601–20,622, doi:10.1029/94JD00819.

Gardner, C. S., and W. Yang (1998), Measurements of the dynamical cooling rate associated with the vertical transport of heat by dissipating gravity waves in the mesopause region at the Starfire Optical Range, New Mexico, *J. Geophys. Res.*, *103*(D14), 16,909–16,926, doi:10.1029/98JD00683.

Gardner, C. S., D. C. Senfit, T. J. Beatty, R. E. Bills, and C. A. Hostetler (1989), Rayleigh and sodium lidar techniques for measuring middle atmospheric density, temperature and wind perturbations and their spectra, in *World Ionosphere/Thermosphere Study Handbook*, vol. 2, edited by C. H. Liu and B. Edwards, pp. 148–187, International Congress of Scientific Unions, Urbana, Ill.

Gardner, C. S., S. J. Franke, W. Yang, X. Tao, and J. R. Yu (1998), Interpretation of gravity waves observed in the mesopause region at Starfire Optical Range, New Mexico: Strong evidence for nonseparable intrinsic (m, ω) spectra, *J. Geophys. Res.*, *103*(D8), 8699–8713, doi:10.1029/97JD03428.

Gelbwachs, J. (1994), Iron Boltzmann factor LIDAR: Proposed new remote-sensing technique for mesospheric temperature, *Appl. Opt.*, *33*, 7151–7156.

Geller, M. A., et al. (2013), A comparison between gravity wave momentum fluxes in observations and climate models, *J. Clim.*, *26*, 6383–6405.

Hauchecorne, A., and M. Chanin (1980), Density and temperature profiles obtained by lidar between 35 and 70 km, *Geophys. Res. Lett.*, *7*(8), 565–568, doi:10.1029/GL007i008p00565.

Hines, C. O. (1960), Internal atmospheric gravity waves at ionospheric heights, *Can. J. Phys.*, *38*, 1441–1481, doi:10.1139/p60-150.

Hines, C. O. (1991), The saturation of gravity waves in the middle atmosphere, II, Development of Doppler-spread theory, *J. Atmos. Sci.*, *48*, 1360–1379.

Hines, C. O. (1997a), Doppler-spread parameterization of gravity-wave momentum deposition in the middle atmosphere, 1, Basic formulation, *J. Atmos. Sol. Terr. Phys.*, *59*, 371–386.

Hines, C. O. (1997b), Doppler-spread parameterization of gravity-wave momentum deposition in the middle atmosphere, 2, Broad and quasi monochromatic spectra, and implementation, *J. Atmos. Sol. Terr. Phys.*, *59*, 387–400.

Holton, J. R. (1982), The role of gravity wave induced drag and diffusion in the momentum budget of the mesosphere, *J. Atmos. Sci.*, *39*, 791–799.

Hu, X., A. Z. Liu, C. S. Gardner, and G. R. Swenson (2002), Characteristics of quasi-monochromatic gravity waves observed with Na lidar in the mesopause region at Starfire Optical Range, NM, *Geophys. Res. Lett.*, *29*(24), 2169, doi:10.1029/2002GL014975.

Lindzen, R. S. (1981), Turbulence and stress owing to gravity-wave and tidal breakdown, *J. Geophys. Res.*, *86*(C10), 9707–9714, doi:10.1029/JC086iC10p09707.

Lu, X., A. Z. Liu, G. R. Swenson, T. Li, T. Leblanc, and I. S. McDermid (2009), Gravity wave propagation and dissipation from the stratosphere to the lower thermosphere, *J. Geophys. Res.*, *114*, D11101, doi:10.1029/2008JD010112.

Lu, X., X. Chu, T. Fuller-Rowell, L. Chang, W. Fong, and Z. Yu (2013), Eastward propagating planetary waves with periods of 1–5 days in the winter Antarctic stratosphere as revealed by MERRA and lidar, *J. Geophys. Res. Atmos.*, *118*, 9565–9578, doi:10.1002/jgrd.50717.

McDonald, A. J., L. Thomas, and D. P. Wareing (1998), Night-to-night changes in the characteristics of gravity waves at stratospheric and lower-mesospheric heights, *Ann. Geophys.*, *16*, 229–237, doi:10.1007/s00585-998-0229-0.

McDonald, A. J., S. E. George, and R. M. Woollands (2009), Can gravity waves significantly impact PSC occurrence in the Antarctic?, *Atmos. Chem. Phys.*, *9*, 8825–8840.

McLandress, C., T. G. Shepherd, S. Polavarapu, and S. R. Beagley (2012), Is missing orographic gravity wave drag near 60°S the cause of the stratospheric zonal wind biases in chemistry–climate models?, *J. Atmos. Sci.*, *69*, 802–818.

Mzé, N., A. Hauchecorne, P. Keckhut, and M. Thétis (2014), Vertical distribution of gravity wave potential energy from long-term Rayleigh lidar data at a northern middle-latitude site, *J. Geophys. Res. Atmos.*, *119*, 12,069–12,083, doi:10.1002/2014JD022035.

Pan, W., and C. S. Gardner (2003), Seasonal variations of the atmospheric temperature structure at South Pole, *J. Geophys. Res.*, *108*(D18), 4564, doi:10.1029/2002JD003217.

Pan, W., C. S. Gardner, and R. G. Roble (2002), The temperature structure of the winter atmosphere at South Pole, *Geophys. Res. Lett.*, *29*(16), 1802, doi:10.1029/2002GL015288.

Pfenninger, M., A. Z. Liu, G. C. Papem, and C. S. Gardner (1999), Gravity wave characteristics in the lower atmosphere at South Pole, *J. Geophys. Res.*, *104*(D6), 5963–5984, doi:10.1029/98JD02705.

Picone, J., A. Hedin, D. P. Drob, and A. Aikin (2002), NRLMSISE-00 empirical model of the atmosphere: Statistical comparisons and scientific issues, *J. Geophys. Res.*, *107*(A12), 1468, doi:10.1029/2002JA009430.

Preusse, P., A. Dörnbrack, S. D. Eckermann, M. Riese, B. Schaeler, J. T. Bacmeister, D. Broutman, and K. U. Grossmann (2002), Space-based measurements of stratospheric mountain waves by CRISTA 1. Sensitivity, analysis method, and a case study, *J. Geophys. Res.*, *107*(D23), 8178, doi:10.1029/2001JD000699.

Preusse, P., et al. (2006), Tropopause to mesopause gravity waves in August: Measurement and modeling, *J. Atmos. Sol. Terr. Phys.*, *68*, 1730–1751.

Preusse, P., S. D. Eckermann, and M. Ern (2008), Transparency of the atmosphere to short horizontal wavelength gravity waves, *J. Geophys. Res.*, *113*, D24104, doi:10.1029/2007JD009682.

Rauthe, M., M. Gerding, J. Höffner, and F. J. Lübken (2006), Lidar temperature measurements of gravity waves over Kühlungsborn (54°N) from 1 to 105 km: A winter-summer comparison, *J. Geophys. Res.*, *111*, D24108, doi:10.1029/2006JD007354.

Rauthe, M., M. Gerding, and F. J. Lübken (2008), Seasonal changes in gravity wave activity measured by lidars at mid-latitudes, *Atmos. Chem. Phys.*, *8*, 6775–6787, doi:10.5194/acp-8-6775-2008.

Sato, K. (1994), A statistical study of the structure, saturation and sources of inertio-gravity waves in the lower stratosphere observed with the MU radar, *J. Atmos. Terr. Phys.*, *56*, 755–774.

Senft, D. C., and C. S. Gardner (1991), Seasonal variability of gravity wave activity and spectra in the mesopause region at Urbana, *J. Geophys. Res.*, *96*, 17,229–17,264, doi:10.1029/91JD01662.

Senft, D. C., C. A. Hostetler, and C. S. Gardner (1993), Characteristics of gravity wave activity and spectra in the upper stratosphere and upper mesosphere at Arecibo during early April 1989, *J. Atmos. Terr. Phys.*, *55*, 499–511.

Smith, S. A., D. C. Fritts, and T. E. Van Zandt (1987), Evidence for a saturated spectrum of atmospheric gravity waves, *J. Atmos. Sci.*, *44*, 1404–1410.

Swinbank, R., and D. A. Ortland (2003), Compilation of wind data for the Upper Atmosphere Research Satellite (UARS) reference atmosphere project, *J. Geophys. Res.*, *108*(D19), 4615, doi:10.1029/2002JD003135.

Tan, B., H.-L. Liu, and X. Chu (2011), Studying the "cold pole" problem in WACCM and comparison to lidar temperature morphology, Abstract SA31B-1973, presented at 2011 Fall Meeting, AGU, San Francisco, Calif., 7 Dec.

Tsuda, T., T. Inoue, D. C. Fritts, T. E. VanZandt, S. Kato, T. Sato, and S. Fukao (1989), MST radar observations of a saturated gravity wave spectrum, *J. Atmos. Sci.*, *46*, 2440–2447.

Van Zandt, T. E. (1982), A universal spectrum of buoyancy waves in the atmosphere, *Geophys. Res. Lett.*, *9*, 575–578, doi:10.1029/GL009i005p00575.

Wang, Z., X. Chu, W. Huang, W. Fong, J. A. Smith, and B. Roberts (2012), Refurbishment and upgrade of Fe Boltzmann/Rayleigh temperature lidar at Boulder for McMurdo lidar campaign in Antarctica, Proceeding of the 26th International Laser Radar Conference, 207–210, Porto Heli, Greece, 25–29 June.

Weinstock, J. (1990), Saturated and unsaturated spectra of gravity waves and scale-dependent diffusion, *J. Atmos. Sci.*, *47*, 2211–2225.

Whiteway, J. A., and A. I. Carswell (1994), Rayleigh lidar observations of thermal structure and gravity wave activity in the high Arctic during a stratospheric warming, *J. Atmos. Sci.*, *51*, 3122–3136.

Whiteway, J. A., and A. I. Carswell (1995), Lidar observations of gravity wave activity in the upper stratosphere over Toronto, *J. Geophys. Res.*, *100*(D7), 14,113–14,124, doi:10.1029/95JD00511.

Wilson, R., M. L. Chanin, and A. Hauchecorne (1991a), Gravity waves in the middle atmosphere observed by Rayleigh lidar 1. Case studies, *J. Geophys. Res.*, *96*, 5153–5167, doi:10.1029/90JD02231.

Wilson, R., M. L. Chanin, and A. Hauchecorne (1991b), Gravity waves in the middle atmosphere observed by Rayleigh lidar 2. Climatology, *J. Geophys. Res.*, *96*, 5169–5183, doi:10.1029/90JD02610.

Yamashita, C., X. Chu, H.-L. Liu, P. J. Espy, G. J. Nott, and W. Huang (2009), Stratospheric gravity wave characteristics and seasonal variations observed by lidar at the South Pole and Rothera, Antarctica, *J. Geophys. Res.*, *114*, D12101, doi:10.1029/2008JD011472.

Yang, G., B. Clemesha, P. Batista, and D. Simonich (2010), Seasonal variations of gravity wave activity and spectra derived from sodium temperature lidar, *J. Geophys. Res.*, *115*, D18104, doi:10.1029/2009JD012367.